frontiers | Frontiers in Earth Science

TYPE Original Research
PUBLISHED 25 October 2022
DOI 10.3389/feart.2022.1029471



OPEN ACCESS

EDITED BY
Marzia Rovere,
Institute of Marine Sciences, Italy

REVIEWED BY
Dong Feng,
Shanghai Ocean University, China
Vitor Hugo Magalhaes,
Portuguese Institute for Sea and Atmosphere (IPMA), Portugal

*CORRESPONDENCE
Claudio Argentino,
claudio.argentino@uit.no

SPECIALTY SECTION
This article was submitted to Marine Geoscience,
a section of the journal
Frontiers in Earth Science

RECEIVED 27 August 2022
ACCEPTED 07 October 2022
PUBLISHED 25 October 2022

CITATION
Argentino C, Lee A, Fallati L, Sahy D, Birgel D, Peckmann J, Bünz S and Panieri G (2022), Biogeochemistry and timing of methane-derived carbonate formation at Leirdjupet fault complex, SW Barents sea.
*Front. Earth Sci.* 10:1029471.
doi: 10.3389/feart.2022.1029471



# Biogeochemistry and timing of methane-derived carbonate formation at Leirdjupet fault complex, SW Barents sea

Claudio Argentino[1]*, Amicia Lee[2], Luca Fallati[3], Diana Sahy[4], Daniel Birgel[5], Jörn Peckmann[5], Stefan Bünz[1] and Giuliana Panieri[1]

[1]CAGE—Centre for Arctic Gas Hydrate, Environment and Climate, Department of Geosciences, UiT The Arctic University of Norway, Tromsø, Norway, [2]Department of Geosciences, UiT The Arctic University of Norway, Tromsø, Norway, [3]Department of Earth and Environmental Sciences, University of Milano-Bicocca, Milano, Italy, [4]British Geological Survey, Nottingham, United Kingdom, [5]Center for Earth System Research and Sustainability, Institute for Geology, Universität Hamburg, Hamburg, Germany

The origin of modern seafloor methane emissions in the Barents Sea is tightly connected to the glacio-tectonic and oceanographic transformations following the last ice age. Those regional events induced geological structure re-activation and destabilization of gas hydrate reservoirs over large areas of the European continental margins, sustaining widespread fluid plumbing systems. Despite the increasing number of new active seep discoveries, their accurate geochronology and paleo-dynamic is still poorly resolved, thus hindering precise identification of triggering factors and mechanisms controlling past and future seafloor emissions. Here, we report the distribution, petrographic (thin section, electron backscatter diffraction), isotopic ($\delta^{13}C$, $\delta^{18}O$) and lipid biomarker composition of methane-derived carbonates collected from Leirdjupet Fault Complex, SW Barents Sea, at 300 m depth during an ROV survey in 2021. Carbonates are located inside a 120 x 220 m elongated pockmark and form <10 $m^2$ bodies protruding for about 2 m above the adjacent seafloor. Microstructural analyses of vein-filling cements showed the occurrence of three–five generations of isopachous aragonitic cement separated by dissolution surfaces indicative of intermittent oxidizing conditions. The integration of phase-specific isotopic analysis and U/Th dating showed $\delta^{13}C$ values between –28.6‰ to –10.1‰ and $\delta^{18}O$ between 4.6‰ and 5.3‰, enabling us to track carbonate mineral precipitation over the last ~8 ka. Lipid biomarkers and their compound-specific $\delta^{13}C$ analysis in the bulk carbonate revealed the presence of anaerobic methanotrophic archaea of the ANME-2 clade associated with sulfate-reducing bacteria of the Seep-SRB1 clade, as well as traces of petroleum. Our results indicate that methane and petroleum seepage in this area followed a similar evolution as in other southernmost Barents Sea sites controlled by the asynchronous deglaciation of the Barents Sea shelf, and that methane-derived carbonate precipitation is still an active process at many Arctic locations.

KEYWORDS

Aom (anaerobic oxidation of methane), authigenic carbonate, cold seep, lipid biomarkers, U/Th, Leirdjupet fault complex, Barents Sea

## Introduction

Natural seafloor methane emissions, known as cold seeps, are common features along continental margins (Phrampus et al., 2020), where vast amounts of methane, trapped in deep subsurface hydrocarbon reservoirs or shallower gas hydrates, migrate through faults or sediments with low permeability pathways toward the surface (Judd and Hovland, 2007; Suess, 2014). Cold seeps are inhabited by peculiar chemosynthetic communities (Sahling et al., 2002; Foucher et al., 2007; Fischer et al., 2012; Levin et al., 2016), including bacterial mats, tubeworms, and bivalves, which are gaining their energy by oxidation of reduced compounds ($HS^-$, $CH_4$) at an otherwise nutrient-poor seafloor (Levin et al., 2016). Despite the fact that cold seeps are widespread along continental margins, they only provide a minor contribution of the global methane emissions, especially when compared to natural land sources (Weber et al., 2019). In fact, ca. 90% of the methane seeping from marine sediments (Hinrichs and Boetius, 2002; Reeburgh, 2007; Knittel and Boetius, 2009) is microbially consumed close to the seafloor by the anaerobic oxidation of methane (AOM) consortium (Boetius et al., 2000). The remaining small fraction of methane escaping the sedimentary bio-filter is almost entirely oxidized by aerobic methane-oxidizing bacteria in the water-column before reaching the sea surface (McGinnis et al., 2006; Sparrow et al., 2018; Jansson et al., 2019). Methane-derived carbon is sequestered into authigenic carbonates precipitating within the sediment due to an alkalinity increase produced by the AOM consortium ($CH_4 + SO_4^{2-} \rightarrow HCO_3^- + HS^- + H_2O$). These carbonates, also known as methane-derived authigenic carbonates (MDAC), are invaluable tools in cold-seep research as they record the fluid composition in which they form and have been extensively used as benchmarks in the development of new geochemical proxies for AOM (Feng et al., 2016; Smrzka et al., 2016; Crémière et al., 2020; Yao et al., 2020) and redox conditions (Himmler et al., 2010; Zwicker et al., 2018; Bayon et al., 2020; Smrzka et al., 2020). These studies allow to provide more accurate reconstructions of sediment biogeochemistry and seepage activity. The $\delta^{13}C$ composition of seep carbonates typically ranges from −60‰ to −30‰ (Judd and Hovland, 2007), mainly reflecting the incorporation of dissolved inorganic carbon (DIC) released by AOM ($\delta^{13}C_{DIC} < -30‰$) and organic matter mineralization ($\delta^{13}C_{DIC} > -30‰$) (Meyers, 1994; Swart, 2015) superimposed by the background seawater DIC signal (~0‰). The $\delta^{13}C$ value of the carbonate tends to be more negative (close to $CH_4$ composition, generally << −30‰), the higher the methane flux and AOM rate. However, oxidation of deeper, thermogenic gas or hydrocarbons have been shown to result in the precipitation of carbonates with heavier $\delta^{13}C$ signatures (Roberts and Feng, 2013). Generally, the $\delta^{18}O$ values of methane-derived carbonates depend on the temperature of precipitation and carbonate mineralogy, but gas hydrate derived water is $^{18}O$-enriched (Davidson et al., 1983) and can lead to anomalously heavy carbonate $\delta^{18}O$ signatures, which are not in isotopic equilibrium with seawater (Bohrmann et al., 1998; Teichert et al., 2005; Bohrmann and Torres, 2006). Such conditions have been reported from many modern cold seeps from gas hydrate bearing areas, e.g. Cascadia Margin (Bohrmann et al., 1998, 2002; Greinert et al., 2013), Gulf of Cadiz (Magalhães et al., 2012), Gulf of Mexico (Roberts and Feng, 2013), Congo Fan (Feng et al., 2010a), Barents Sea (Crémière et al., 2016; Argentino et al., 2021; Yao et al., 2021); the $\delta^{18}O$ proxy has been applied to fossil seep carbonates as well (Pierre and Rouchy, 2004; Campbell, 2006; Campbell et al., 2008; Argentino et al., 2019; Bojanowski et al., 2021). Owing to their microbial origin, seep carbonates incorporate and harbor typical communities of methane-oxidizing archaea and sulfate-reducing bacteria (Marlow et al., 2014). Eventually, the prokaryotes involved in AOM leave behind detectable organic traces in the lipid biomarker inventory of the rock that can be preserved for hundreds of millions of years in the sedimentary record (Peckmann and Thiel, 2004; Birgel and Peckmann, 2008) providing insights into AOM dynamics and microbial ecology (Peckmann et al., 2009; Kim and Zhang, 2022). Finally, the timing of carbonate formation at modern seeps (<500 ka BP) can be determined with a precision in the order of $\pm10^2$–$10^3$ y *via* Uranium/Thorium (U/Th) dating (Teichert et al., 2003; Feng et al., 2010b; Himmler et al., 2019). The absolute dating of seep carbonates is essential to reconstruct the high-resolution history of seepage, enabling geoscientists to determine the evolution of seepage over critical climatic phases of Earth history, which can help predict future global warming scenarios.

Cold seep research conducted over the years in the Barents Sea (Crémière et al., 2016; Andreassen et al., 2017; Serov et al., 2017; Yao et al., 2020) and other Arctic paleo-glaciated margins (Portnov et al., 2016; Schneider et al., 2018; Himmler et al., 2019; Kravchishina et al., 2021) revealed episodes of massive seafloor gas seepage following deglaciations. These events are highlighting the role of grounded ice sheets as “capacitors” facilitating the storage of methane into sub-glacial gas hydrates and inducing large-scale release upon ice retreat. Arctic paleo-systems are considered good analogs to modern western Antarctica and Greenland settings (Elverhøi et al., 2002; Esteves et al., 2017), where ongoing and projected ice-sheet retreat might lead to the development of widespread methane seeps sourced by underlying hydrocarbon reservoirs and gas hydrates. Consequently, understanding the timing and dynamics of

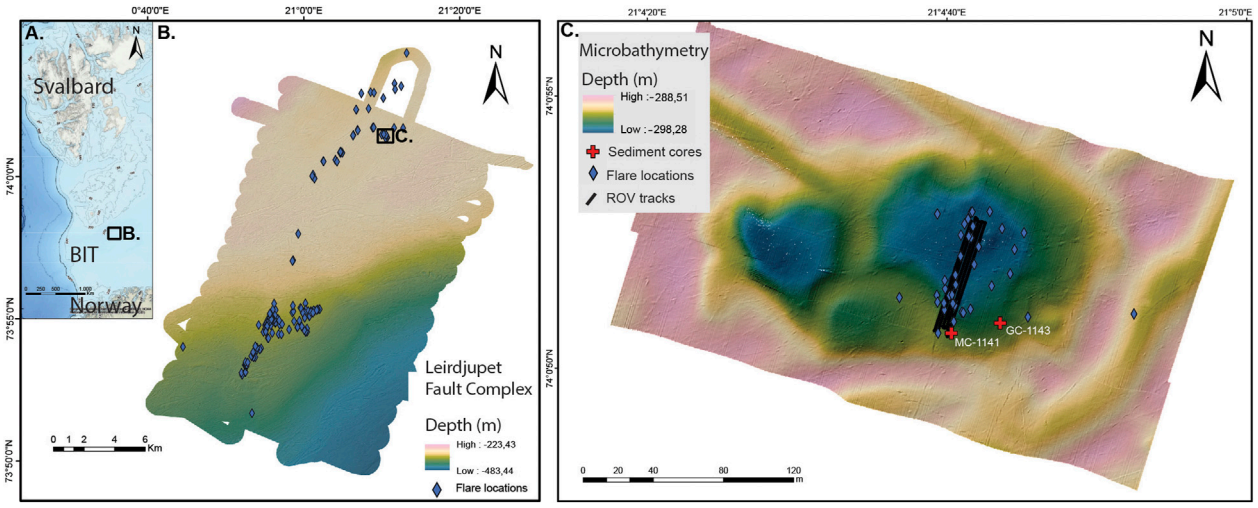


FIGURE 1
**(A)** Bathymetric map of the Western Barents Sea showing the location of the study area (box). **(B)** Distribution of gas flares (polygons) at Leirdjupet Fault Complex and location of the pockmark site (box). **(C)** Microbathymetry of the pockmark site showing ROV tracks used for the photogrammetry survey in the methane-derived carbonate area, location of flares and two sediment cores previously reported in Argentino et al. (2021). BIT = Bear Island Trough. This color scale is accessible for people with color-vision deficiencies (Crameri et al., 2020).

seepage throughout deglaciations in paleo-glaciated margins is essential to better predict future scenarios and greenhouse fluxes into the hydrosphere and atmosphere at modern glaciated margins. Extensive research conducted in the last decade was undertaken to map the distribution of seeps in the western Barents Sea, leading to the discovery of widespread methane emissions mostly occurring in its southern sector, but especially associated with major hydrocarbon fields of economic relevance (Chand et al., 2012; Crémière et al., 2016, 2018). Subsurface seismic features consisting of fluid/gas chimneys, pipes, faults, buried pockmarks and gas-hydrate-related bottom-simulating reflectors (BSR) provided evidence for a well-developed fluid-flow system fed by microbial and thermogenic gas leakage from Mesozoic reservoirs (Vadakkepuliyambatta et al., 2013, 2017). Methane seepage-derived carbonates collected from the seafloor at some active locations (Crémière et al., 2016, 2018) were essential to resolve the geochronology of seepage in the SW Barents Sea and correlate episodes of major gas emissions with deglacial history of the Barents Sea Ice Sheet. Methane seeps have been recently discovered and reported from other sectors of the SW Barents Sea (Andreassen et al., 2017; Waage et al., 2020; Argentino et al., 2021). Their temporal constraints on when the major seepage activity was remains poorly resolved, thus hindering a more precise identification of the triggering factors and mechanisms controlling the evolution of seafloor emissions throughout deglaciation. Filling this gap would allow us to establish a comprehensive reconstruction of the spatial and temporal relationships between ice-sheet retreat and seafloor methane emissions along the whole western Barents Sea, connecting the southernmost sites close to the Norwegian mainland (Sauer et al., 2015; Crémière et al., 2016, 2018) to the seeps located in the NW Barents Sea (Hong et al., 2017) and W Svalbard (Panieri et al., 2017; Himmler et al., 2019), providing the means to interpret the evolution of modern glaciated counterparts affected by global warming.

We investigated carbonate crusts collected during a survey with a remotely operated underwater vehicle (ROV) in 2021 at Leirdjupet Fault Complex, SW Barents Sea (Figure 1A). Carbonates are exposed at the seafloor inside a pockmark feature, located on an active ~30 km long fluid seepage system (Argentino et al., 2021) (Figure 1B). ROV multibeam echosounder surveys enabled us to obtain micro-bathymetry of the seafloor of the pockmark area (Figure 1C), and the ROV photogrammetry allowed us to generate high-resolution orthomosaic and 3D models of carbonate outcrops. We conducted petrographic and microstructural (Electron Backscatter Diffraction) investigations of rock samples and then selected pure aragonite cements for phase-specific isotopic analysis $\delta^{13}C$, $\delta^{18}O$ and U/Th dating. Lipid biomarkers and their compound-specific $\delta^{13}C$ values were used to characterize microbial communities preserved in authigenic carbonates for the first time in this area to provide deeper insights into AOM dynamics. This study provides the first absolute temporal constraints on the inception and evolution of seepage at Leirdjupet Fault Complex, which may be used as key site to extrapolate the relative magnitude and timing of past methane emissions along the whole western Barents Sea margin by correlation.

## Study area

The Leirdjupet Fault Complex (LFC) is located on a transverse shelf trough named Bear Island Trough, in the SW Barents Sea (Figure 1A). The fault complex was first visited by CAGE in 2017 for hydroacoustic exploration and at that time methane seepage was detected along a ~35 km transect striking NE-SW making LFC one of the most active areas in the SW Barents Sea (Figure 1A). Water depths within the explored area range from 220 m to 400 m and the seafloor morphology is marked by ploughmarks and moraines related to the glacial dynamics of the Late Weichselian Barents Sea Ice Sheet, which covered the Bear Island Trough until ~15 ka BP (Winsborrow et al., 2010; Patton et al., 2017). In 2018, seafloor observations using a tow-camera-multicorer system allowed to describe and map the habitat distributions and their relationships with subsurface methane fluxes (Argentino et al., 2022). Active seeps are characterized by white patches of bacterial mats surrounded by frenulate siboglinids thriving on methane and AOM-related hydrogen. The analysis of fluids emitted at the seafloor indicated a mix of thermogenic and microbial gas derived from Mesozoic reservoirs and shallower Tertiary deposits, sustaining the formation of shallow gas hydrate reservoirs during ice ages and eventually destabilized by late deglaciation (Argentino et al., 2021). Recently, the AKMA-CAGE21-1 expedition visited the LFC area on R/V Kronprins Haakon in 2021 with the ROV Ægir6000 for high-resolution seafloor imaging and targeted samplings of seabed features, i.e. sediments, rocks. The carbonate samples investigated for this study were collected from an elongated 120 x 220 m seafloor depression at 300 m depth previously interpreted as a pockmark (Argentino et al., 2021) and located in the northern sector of LFC (Figure 1B). The pockmark is composed of three smaller seafloor depressions, the largest of which is located to the north-eastern corner and is currently the most active in terms of the number of methane flares (Figure 1C), and for that reason it was selected for ROV photogrammetry and samplings.

## Methods

### Seafloor imagery acquisition and processing

ROV Ægir6000, equipped with a dedicated photogrammetry sledge, explored the most active part of the pockmark. This setting allowed to acquire high-definition videos parallel to the seafloor. The ROV, moving at a constant speed of 0.5 knots, followed four predefined 70 m long transects with an altitude of 2 m to guarantee optimal lateral overlap between adjacent tracks. A photogram every 2 s was automatically extracted from the nadiral camera's videos. Then, the images were processed in Agisoft Metashape®, following a well-established photogrammetry workflow (Fallati et al., 2020; Montalbetti et al., 2022). As final outputs a 3D mesh, orthomosaics and Digital Terrain Models (DTMs) at high-resolution were obtained, allowing us to get detailed morphometric parameters of the carbonate outcrops at a cm-scale resolution.

### Carbonate sampling

Methane-derived carbonate CAGE21-1-KH-05_Dive19-CarC-05, hereafter named CarC-05, was collected from a carbonate slab exposed at the seafloor using the ROV manipulating arm. On deck, the sample was subsampled for macrofauna, washed with freshwater to remove salt residues and stored at 4°C. The carbonate rock was sawed onshore at UiT-The Arctic University of Norway and split into rock chips for thin section preparation. Thin sections CarC-05-A and CarC-05-C were analyzed *via* optical microscopy for carbonate microfacies description and CarC-05-C was selected for mineralogical characterization *via* scanning electron microscopy—Electron Backscatter Diffraction (EBSD). A total of three generations of cavity-filling cements were sampled from CarC-05-1C using a hand-held microdrill and subjected to U/Th dating and $\delta^{13}C$ and $\delta^{18}O$ analyses. The subsamples are named CarC-05-C-*1*, CarC-05-C-*2* and CarC-05-C-*3*. Lipid biomarker analysis were conducted on bulk rock material of CarC-05. In this study we also report the isotopic composition of cm-sized carbonate concretions found in gravity core CAGE18-4-HH-GC-1143 at 4 cm below the seafloor (bsf) and multicore CAGE18-4-HH-MC-1141 at 18 cm and 26 cm bsf, collected in 2018 from the same pockmark (Argentino et al., 2021), and hereafter named GC-1143, MC-1141a and MC-1141b.

### Scanning electron microscopy—Electron backscatter diffraction (EBSD)

Crystallographic orientation data was collected *via* electron backscatter diffraction (EBSD) with an Oxford Instruments Nordlys S detector on a Zeiss Merlin SEM at The Arctic University of Norway in Tromsø. Crystallographic data were collected using 20 kV accelerating voltage, 70° specimen tilt angle and 22–26 mm working distance. Detailed maps were measured with a step size of 8–15 µm and seven bands detected. Oxford Instruments Aztec software was used for data acquisition and initial data processing, MTEX v.5.7.0 open source software toolbox (Bachmann et al., 2010) for MATLAB was used for enhanced data processing and pole figure plotting. Individual crystal orientations with median absolute deviation (MAD) values >1.0 were removed.

## Stable isotope geochemistry ($\delta^{13}C$, $\delta^{18}O$) and U/Th geochronology

The stable isotope composition ($\delta^{13}C$, $\delta^{18}O$) of carbonate samples was measured on a Thermo Scientific Gasbench II coupled to a Finnigan MAT 253 triple collector isotope ratio mass spectrometer at the Stable Isotope Lab-SIL of UiT, after reaction with anhydrous phosphoric acid for 3 h at 50°C. Data are reported in ‰ notation relative to Vienna Pee Dee belemnite (V-PDB). Analytical error was better than 0.1‰ (1SD) for both carbon and oxygen.

U/Th dating was conducted at the British Geological Survey's Geochronology and Tracers Facility, following the protocol outlined by Crémière et al. (2016). U and Th were measured on a Thermo Neptune Plus multicollector ICP-MS using a $^{236}$U-$^{229}$Th isotopic tracer. Instrument parameters were monitored using CRM112a and IRMM3636 uranium and an in-house $^{229}$Th-$^{230}$Th-$^{232}$Th reference solution as bracketing standards. A correction was applied to account for the presence of intial deterital/hydrogenous $^{230}$Th based on values reported by Crémière et al. (2016) from MDAC-free background sediment samples from a similar water depth range as covered in this study. U/Th activity ratios are reported in Supplementary Table S1.

## Lipid biomarkers and compound-specific isotope analysis ($\delta^{13}C$)

125 g of bulk material from CarC-01 was crushed, then decalcified by slowly pouring 10% HCl onto the sample, until 80 wt% of the sample was dissolved. The material collected after decalcification was saponified with 6% KOH in methanol to release bound fatty acids and extracted by using dichloromethane/methanol (3:1 volume). Prior to saponification and extraction, 200 µL of five α (H)-cholestane, 1-nonadecanol, and 2-methyl-octadecanoic acid were added as internal standards. The combined total lipid extracts (TLE) were then separated into maltenes (*n*-hexane soluble) and asphaltenes (dichloromethane). The maltenes were further separated with a $NH_2$-modified silica gel column into four fractions with of increasing polarity: hydrocarbons (fraction 1), ketones/esters (fraction 2), alcohols (fraction 3) and carboxylic acids (fraction 4). Fractions three and four were derivatized using N,N-*bis* trimethylsilyltriflour(o)acetamide(s) (BSTFA) and boron trifluoride (BF3)/MeOH, respectively and analyzed *via* gas chromatography-mass spectrometry (GC-MS) using an Agilent 7890 A GC system coupled to an Agilent 5975C inert MSD mass spectrometer at the University of Hamburg. Compound-specific stable carbon isotope analyses were determined using a Trace GC Ultra linked *via* a Thermo Finnigan Combustion interface with a Finnigan MAT 252 isotope mass spectrometer (GC-IRMS) at MARUM, University of Bremen. The GC-MS was equipped with a Thermo Fisher TG-5 MS fused silica column (length: 30 m; inner diameter: 0.25 mm, 0.25 µm film thickness). The GC temperature program used for GC-MS runs was: injection at 50°C, 3 min isothermal; from 50°C to 325°C at a ramp of 6°C $min^{-1}$; 25 min isothermal. The carrier gas was helium. The GC-IRMS was equipped with an Agilent HP-5MS capillary column (length: 30 m; inner diameter: 0.25 mm, 0.25 µm film thickness), the temperature program was: injection at 120 °C, 3 min isothermal, from 120 °C to 320 °C at 5 °C/$min^{-1}$, then held for 15 min $\delta^{13}C$ values are reported in per mil notation relative to Vienna Pee Dee belemnite (V-PDB) standard. Accuracy and precision were determined by analyses of an external *n*-alkane standard calibrated against the A4 mix isotope standard (Arndt Schimmelmann, Indiana University).

# Results

## Seafloor observations in the carbonate area

High-resolution seafloor observations from the ROV survey conducted in the pockmark during AKMA-CAGE21-1 expedition enabled us to obtain information regarding the modality of formation of methane-derived carbonates in relation to methane seepage and the implications for seafloor ecosystems. Thanks to the ROV photogrammetry, georeferenced digital models of 560 $m^2$ of the pockmark seafloor were obtained. The high-resolution photographs of the orthomosaic (Figure 2A) and the DTM (4 mm/pix) (Figure 2B) allowed to describe the carbonate outcrops and the surrounding environments accurately. Carbonate outcrops on the seafloor display a recurring stratiform morphology (Figures 2B–D), consisting of plane-parallel strata with average thickness of 20–30 cm piled up locally to form small (<10 $m^2$ wide) bodies protruding up to 2 m above the adjacent seafloor. Boulder-size blocks are commonly found at the base of these features (Figure 2E). The carbonate deposits are colonized by filter feeders, i.e. anemones and sponges, and offer shelter to higher organisms, i.e. fishes, within large cavities and under carbonate slabs protruding above the seabed (Figure 2E, F, G). Bacterial mats form small white patches (<1 $m^2$ wide) distributed along the outer rims of carbonate deposits and around the bubbling spots on the carbonates (Figures 2E, F). The transition from the carbonate outcrops to the flat background seafloor is sharp and marked by an evident decrease in macrofauna abundance.

## Petrography and EBSD microanalysis

LFC carbonate sample CarC-05 is composed of a dark brown microcrystalline carbonate enclosing fine grained

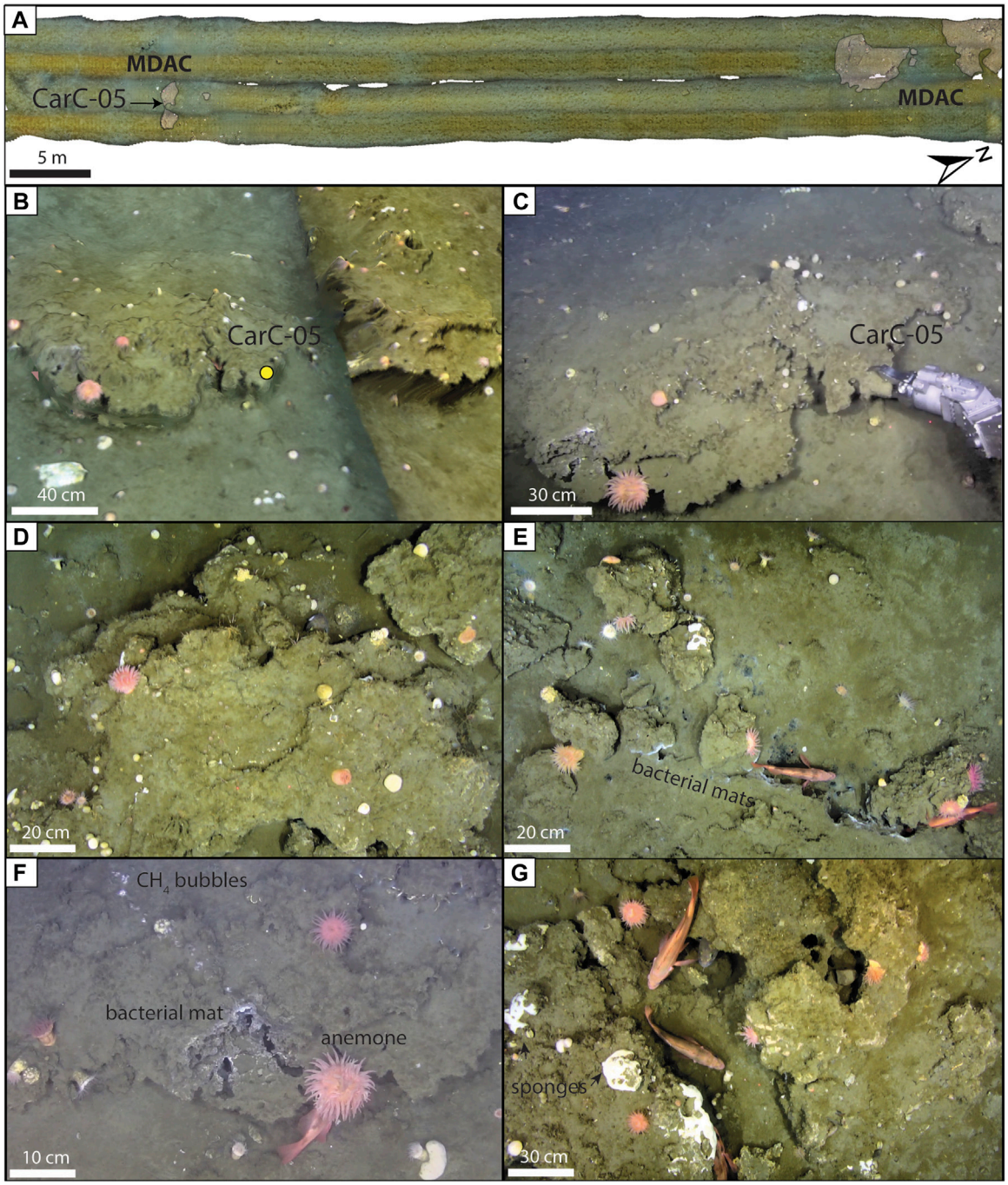


FIGURE 2
Seafloor observations of the carbonate outcrops acquired during AKMA-CAGE21-1 expedition. **(A)** Orthomosaic of the ROV transect across the carbonate outcrops. Carbonate bodies are highlighted with pale color. **(B)** 3D mesh of the carbonate outcrops from which the CarC-05 was collected. **(C)** Sampling of carbonate sample CarC-05 from a stratified carbonate body using the ROV manipulator arm (front camera). **(D)** Stratified carbonate deposits; three layers can be recognized (ortho camera). **(E)** Bacterial mats colonized the outer rim of the carbonate. Some boulders are found at the base of the carbonate structure (ortho camera). **(F)** Bacterial mat around a bubbling spot through the carbonate. Methane bubbles are visible in the photograph. Large anemones are distributed on top and on the rim of the carbonate layers (front camera). **(G)** Anemones and sponges on a carbonate; fishes hiding in cavities within the carbonate body (ortho camera).

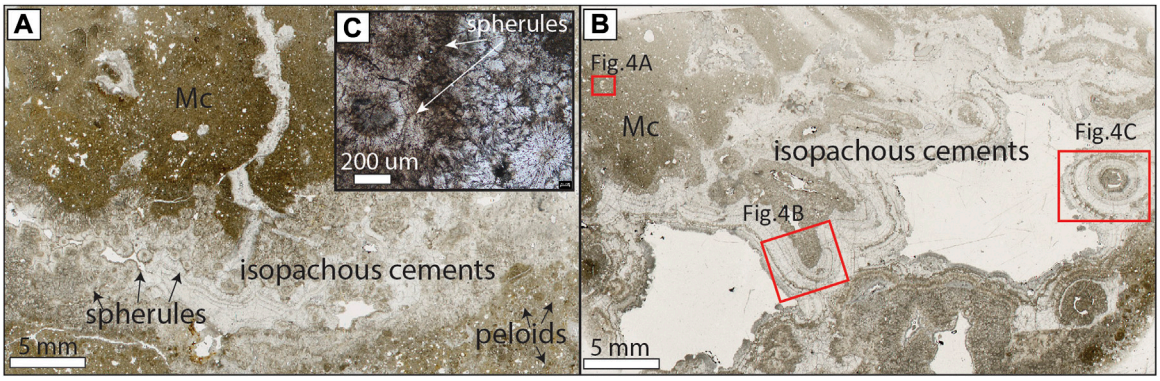


FIGURE 3
Thin section scans from sample CarC-05 collected from the top of a carbonate body. **(A)** Thin section CarC-05-*A* displaying a dark-brown microcrystalline carbonate (Mc) locally displaying peloidal features and crosscut by veins filled by isopachous cements. **(B)** Thin section CarC-05-*C* showing the areas analyzed *via* EBSD, targeting microcrystalline carbonate and isopachous cements **(C)** Close-up view of microcrystalline spherules.

siliciclastic particles of quartz and feldspars. Within the micrite, we identified a peloidal fabric (Figure 3A). Individual peloids are 200–300 μm in diameter and show a microcrystalline composition and regular circular section. The microcrystalline facies is crosscut by veins filled by three–five generations of isopachous cement separated by surfaces showing an irregular outline and locally coated by a thin layer of opaque material, here interpreted as dissolution surfaces (Figure 3B). Early cement phases often engulf microcrystalline spherules with diameters ~100 μm (Figure 3C), generating a mottled microfabric, whereas later stage phases are generally clean. Spherules are pale white colored and display an irregular shape compared to peloids. EBSD investigations indicated that all authigenic carbonate phases in CarC-05 are composed of aragonite (Figure 4). The phase map in Figure 4A shows a dominant aragonitic mineralogy of the microcrystalline carbonate of the matrix engulfing a low magnesium calcite foraminiferal test. EBSD analysis also revealed a secondary high magnesium carbonate phase (calcite or dolomite) overgrowth on the test. Crystal orientation data are represented through an orientation map located to the right side of Figure 4A. The orientation map of the microcrystalline matrix shows randomly oriented microcrystals, similarly to what was typically found in altered biogenic materials (Cusack et al., 2008; Casella et al., 2018). The orientation map of the isopachous cements and the pole figures highlight a strong crystallographic relationship between neighboring grains (orientation axis) (Figures 4B,C). Dissolution surfaces between cement phases are associated with some empty spaces in the orientation map due to absence of diffraction. Misorientation maps have been prepared to highlight areas where the crystal orientations deviate from the grain average (Supplementary Figure S1). To the best of our knowledge this is the first application of EBSD analysis to methane-derived carbonates.

## Isotope composition ($\delta^{13}C$, $\delta^{18}O$) and U/Th ages

The carbon isotope composition of fibrous aragonite cements CarC-05-C-*1*, CarC-05-C-*2* and CarC-05-C-*3* shows, in spite of only three sample points being used, a trend toward higher $\delta^{13}C$ values passing from earlier phases to later cements (Table 1). Sample CarC-05-C-*1* has the lowest $\delta^{13}C$ values of −28.6‰ and is associated with $\delta^{18}O$ = 5.3‰. The U/Th age of this phase is 8.223 ± 0.229 ka BP, indicating carbonate precipitation during the Early Holocene. Sample CarC-05-C-*2* has a $\delta^{13}C$ = −27.0‰ and $\delta^{18}O$ = 4.6‰; U/Th analysis yielded an age of 7.976 ± 0.248 ka BP. Sample CarC-05-C-*3* shows a $\delta^{13}C$ = −10.1‰ and $\delta^{18}O$ = 5.0‰ and is associated with a U/Th age of 4.087 ± 1.547 ka BP. The contact between this phase and CarC-05-C-*2* is marked by a major dissolution surface making this U/Th age not suitable for extrapolating average growth rates due to unconstrained hiatus. Assuming a linear distance of 0.8–1 mm between the microdrilling spots of CarC-05-C-*1* and CarC-05-C-*2* (center of the cement), and putatively short episode of carbonate dissolution occurred (Figure 4C), the average growth rate ranges were between 3.24 mm/ka and 4.05 mm/ka. The overall $\delta^{13}C$ composition of vein cements is heavier than microcrystalline carbonate concretions from nearby sediment cores GC-1143 and MC-1141, which range from −31.5‰ to −30.0‰; the oxygen signatures of the latter show a narrow range from 5.0‰ to

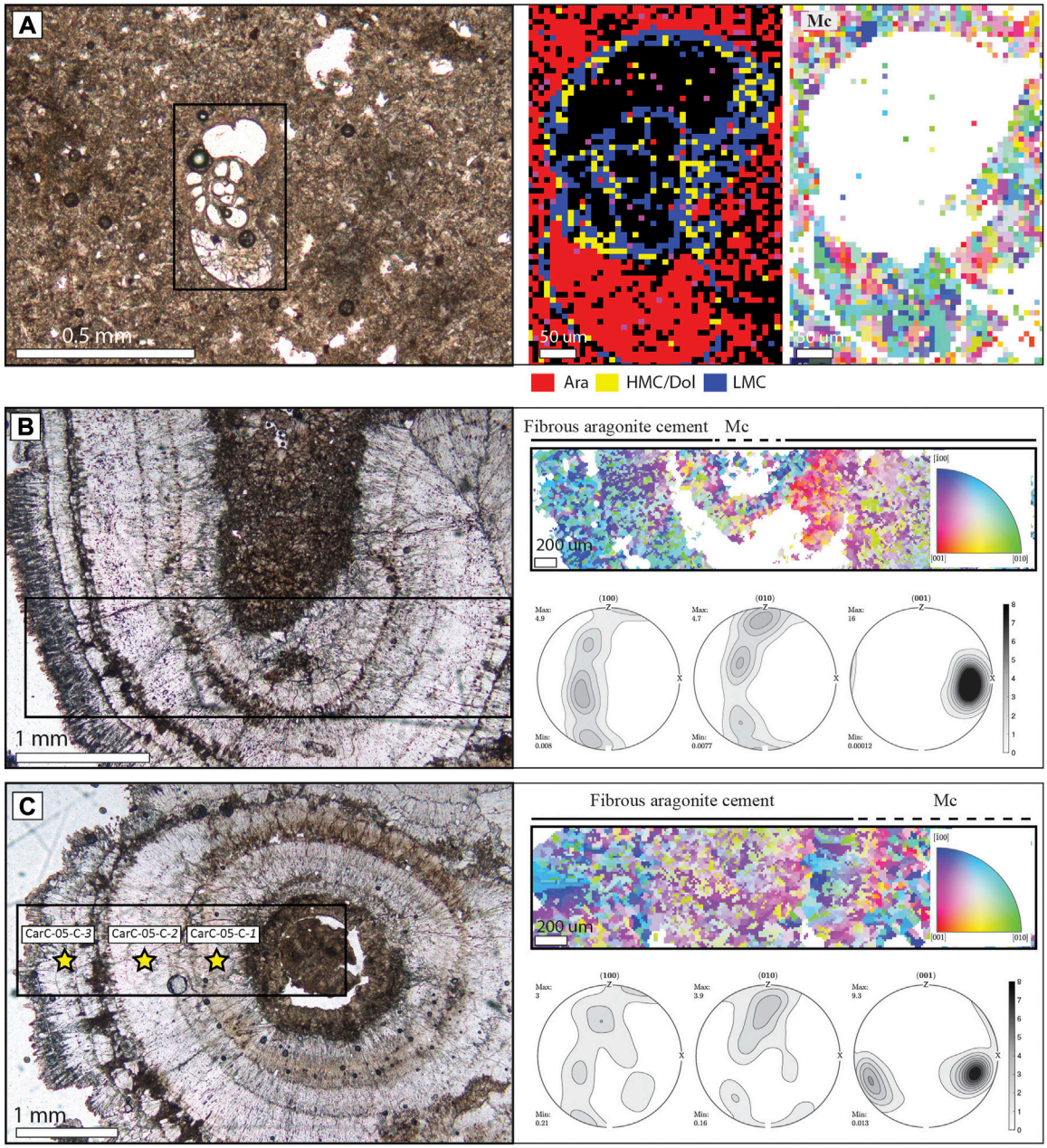


FIGURE 4
Thin section micrographs and EBSD phase and crystal orientation maps of areas marked in Figure 3B. Orientation maps help visualize crystal directions normal to the plane of observation using the color key in the insets. Orientations are also plotted as stereographic projections in the pole figures. **(A)** Micrite microfacies engulfing a foraminiferal test. The EBSD phase map clearly shows a dominant aragonitic mineralogy for the microcrystalline carbonate, with low magnesium calcite corresponding to the test. Some low magnesium calcite/dolomite is found on the test. Microcrystalline carbonate shows randomly-oriented microcrystals in the orientation map. **(B)** Fibrous aragonite cements showing variable orientation of the individual crystals passing from a preferred [–100] crystal direction on the left side of the section to [001] on the right. Cement phases are separated by dissolution surfaces. **(C)** Isopachous cements showing a rather constant crystal orientation close to [–100] direction. The micro-drilled subsample locations are showed with starts. Mc= microcrystalline carbonate.

TABLE 1 Isotopic composition of methane-derived carbonates from Leirdjupet Fault Complex and U/Th ages.

| Sample | Texture | Phase | $\delta^{13}C$ (‰) | $\delta^{18}O$ (‰) | U/Th age (ka BP) |
|---|---|---|---|---|---|
| CarC-05-C-*1* | Fibrous cement | Ara | −28.6 | 5.3 | 8.223 ± 0.229 |
| CarC-05-C-*2* | Fibrous cement | Ara | −27.0 | 4.6 | 7.976 ± 0.248 |
| CarC-05-C-*3* | Fibrous cement | Ara | −10.1 | 5.0 | 4.087 ± 1.547 |
| GC-1143* | Mc | Ara | −30.0 | 5.0 | n.d |
| MC-1141a* | Mc | Ara/HMC | −31.0 | 5.3 | n.d |
| MC-1141b* | Mc | Ara/HMC | −31.5 | 5.0 | n.d |

Mc=microcrystalline carbonate; Ara = aragonite; HMC, high-Mg calcite; n. d. = not determined; *after Argentino et al., 2021.

TABLE 2 Results from lipid biomarker analysis of methane-derived carbonate CarC-05.

| Compound | $\delta^{13}C$ (‰) | Concentration ng/g rock | Source |
|---|---|---|---|
| Hydrocarbons | | | |
| crocetane/phytane | −111 | 292 | ANME |
| PMI | −107 | 137 | ANME |
| *n*-alkanes | −29.3 | 628 | — |
| Σ hydrocarbons | — | 1096 | — |
| Alcohols | | | |
| archaeol | −122 | 1432 | ANME |
| sn2-hydroxy-archaeol | −121 | 2896 | ANME |
| Σ alcohols | — | 5386 | — |
| Fatty acids | | | |
| *iso*-$C_{15}$ | −102 | 82 | SRB |
| *anteiso*-$C_{15}$ | −102 | 143 | SRB |
| Σ fatty acids | — | 1235 | — |
| Proxies | | Information | |
| OH-Ar/Ar | 2.0 | ANME-2 | — |
| *ai*/*i* $C_{15}$-FA | 1.7 | Seep-SRB1 | — |
| $CPI_{23-33}$ | 0.95 | oil-derived alkanes | — |

Concentration (ng/g rock) of the most representative lipid biomarkers of AOM-related archaea (ANME) and sulfate-reducing bacteria (SRB) in carbonate sample CarC-05, and their compound-specific isotopic composition; PMI, pentamethylicosane; DAGE, dialkyl glycerol diether. Full datasets are reported in the Supplementary Table S2.

5.3‰, similar to the values obtained from aragonite cements CarC-05-C-*1* and CarC-05-C-*3*.

## Lipid biomarkers

The total lipid biomarker content of the carbonate sample was 7.7 μg/g rock lipids, where the majority of compounds was found in the alcohol fraction (70 wt%), followed by fatty acids (16 wt%), and hydrocarbons, which comprised 14 wt%. Table 2 reports representative AOM-related biomarkers, whereas the complete datasets are reported in Supplementary Table S2. The hydrocarbon fraction was dominated by *n*-alkanes ranging from *n*-$C_{15}$ to *n*-$C_{33}$, and comprising ca. 60% of all compounds in the hydrocarbon fraction (Table 2). The tail-to-tail linked isoprenoid crocetane is co-eluting with the minor head-to-tail linked isoprenoid phytane (<10% of all hydrocarbons); together with the tail-to-tail linked isoprenoid pentamethlyicosane (PMI) they make up 39.2% of the hydrocarbon fraction (Table 2). The $\delta^{13}C$ value of the mixed crocetane/phytane is −111‰, the value of PMI is −107‰. The head-to-tail linked isoprenoid pristane is a only minor component (38.4 ng/g) and carries an isotopic composition of −30‰ (Supplementary Table S2). *n*-Alkanes (*n*-$C_{15}$-*n*-$C_{33}$) had $\delta^{13}C$ values varying between −34.5‰ and −27.4‰ (average $\delta^{13}C$ = −29.3 ± 1.5‰; N = 19) (Table 2), with *n*-$C_{23}$ showing the most depleted value (Supplementary Table S2). The alkane distribution shows no odd-to-even carbon number preference, resulting in a $CPI_{23-33}$ (Marzi et al., 1993) value of 0.95. The compounds in the alcohol fraction are dominated by the two

archaeal isoprenoid alcohols archaeol (Ar) and *sn*2-hydroxy-archaeol (OH-Ar), comprising 80% of all compounds in the alcohol fraction. Both compounds show low $\delta^{13}C$ values of −122‰ (Ar) and −121‰ (OH-Ar) (Table 2). Putative degradation products of the two archaeols are the *sn*2-and *sn*3-phytanyl-monoether isoprenoids, found with very minor contents of 17.6 ng/g and 22.3 ng/g and $\delta^{13}C$ values of −122‰ and −120‰, respectively. Further compounds in the alcohol fraction were bacterial, non-isoprenoid dialkyl glycerol diether lipids (DAGEs), which comprised ca. 15% of all alcohols and $\delta^{13}C$ values ranging from −121‰ to −98‰. The fatty acid fraction contained fatty acids with chain lengths from $C_{12}$ to $C_{18}$ and a total content of 1,234.6 ng/g. Fatty acids are composed of saturated and unsaturated *n*- and branched fatty acids of bacterial origin. Among the most abundant fatty acids were *iso*- and *anteiso*-$C_{15}$ fatty acids with contents of 82.3 ng/g and 143.2 ng/g, respectively; both are $^{13}C$-depleted with $\delta^{13}C$ values of −102‰. Most $^{13}C$-depleted fatty acids were *n*-$C_{14:1}$ and *iso*-$C_{16}$, revealing contents of 11.6 ng/g and 46.9 ng/g and $\delta^{13}C$ values of −117‰ and −110‰, respectively (Table 2). Phytanoic acid has also been detected with a $\delta^{13}C$ value of −107‰.

# Discussion

## Carbonates reveal diffuse fluid flow

The seafloor observation of methane-derived carbonates from decades of seep research at continental margins indicated a few recurring morphologies mainly controlled by subsurface fluid distributions (diffuse vs. focused flow) and interactions between carbonates and fauna (Campbell, 2006; Judd and Hovland, 2007; Suess, 2014, 2018). Chemoherms are carbonate build-ups growing into the water column due to the accumulation and cementation of biogenic material, i.e. shells of chemosymbiotic bivalves, layers of microbial mats. These structures can reach remarkable lengths of up to 200 m and heights of tens of meters, reflecting spatially-localized activity protracting for several thousands of years. Examples of seep deposits projecting into the bottom water have been reported from Hydrate Ridge (Greinert et al., 2001; Teichert et al., 2005) and the Black Sea (Michaelis et al., 2002), while fossil analogs have been discovered in ancient accretionary prisms and fore arc settings such as the northern Apennine chain in Italy (Aharon, 1994; Conti and Fontana, 1999; Cau et al., 2015) and the East Coast Basin, New Zealand (Campbell et al., 2008). Another more common type of deposit are the so called "carbonate pavements", a term referring to stratiform carbonate deposits forming hardgrounds on the seafloor (Suess, 2014). These deposits form at or close to the sediment-seawater interface and testify for a more diffuse seepage inducing the precipitation of authigenic carbonates over wide areas marked by shallow sulfate-methane transitions (Pierre and Fouquet, 2007; Panieri et al., 2017). Differently from chemoherms representing spatially-localized fluid escape features with high topographic relief and limited lateral extent, e.g., Hydrate Ridge (Teichert et al., 2005), carbonate pavements can reach several thousands of $m^2$ in extent and generally show rather flat or mound-like morphologies (Judd et al., 2020). At the seafloor, vertically-stacked carbonate slabs can form mound-like buildups of a few meters in height locally (Roberts and Feng, 2013; Pierre et al., 2017). These carbonate deposits form an efficient seal to upward migrating fluids and record various episodes of fracturing and cementation caused by gas accumulations beneath the deposits (Loher et al., 2018). Based on the seafloor observations we ascribe the Leirdjupet Fault Complex carbonates to the latter type of deposits. ROV surveys in the pockmark area highlighted the presence of carbonate hardgrounds exploited as substrate by sessile fauna (Figure 3). Bacterial mats and active methane bubbling only occur associated with cm-sized orifices within the carbonates and around the outer rim of the slabs, pointing toward and effective sealing behavior of the deposits at this site. At LFC, methane-rich fluids coming from underlying faulted successions (Argentino et al., 2021) encounter a carbonate cap in the shallow sedimentary column (meters), channeling the fluids into small conduits within the MDAC or deviating them laterally toward their boarder. Bacterial mats colonize the areas on the seafloor where sulfate-driven anaerobic oxidation of methane generates sulfidic conditions and are therefore a reliable proxy for high methane fluxes (Argentino et al., 2022). Based on the geometries and spatial distribution of carbonate outcrops and chemosynthetic communities at the seafloor observed during the ROV dive at this site (Figure 1B), we believe that the carbonate deposits cropping out of the seafloor represents only a minor portion of the whole deposits, mostly buried beneath the sediment-water interface and possibly extending beyond the 560 $m^2$ of data coverage.

## Biogeochemistry of methane-derived carbonates at LFC

Petrographic and microstructural analysis of carbonate sample CarC-05 collected from a stratiform deposit at the seafloor (Figure 3A) revealed a dynamic history of mineral precipitation and dissolution. The sample is composed of microcrystalline aragonite crosscut by veins filled by isopachous cements consisting of fibrous aragonite (Figure 4). The contact between the veins and the enclosing matrix is smooth and regular indicating fluid intrusion through the micrite during an early semi-lithified stage. The aragonite mineralogy of CarC-05 reflects precipitation close to the seafloor, due to the kinetic inhibition of sulfate on calcite precipitation (Mayorga et al., 2019) or, more likely, the lack of sulfide catalysis favoring Mg calcite and dolomite formation (Lu

et al., 2018), and therefore is an indicator of a shallow sulfate-methane transition zone and intense AOM. The presence of high magnesium calcite in cm-sized concretions in sediment core MC-1141 at 18 cm bsf and 26 cm (Argentino et al., 2021), on the other hand, reflects a deeper zone of formation characterized by lower sulfate and higher sulfide pore water concentration gradients at the periphery of the pockmark (Figure 1C). High AOM rates during the precipitation of sample CarC-05 are also testified by its biomarker inventory, especially by the high abundance of the $^{13}$C-depleted isoprenoid crocetane ($\delta^{13}C$= −111‰) and an OH-Ar/Ar ratio >1.1. Both indicators are typical of methanotrophic *Methanosarcinales* of the subgroup ANME-2 (Hinrichs et al., 2000; Niemann and Elvert, 2008) (Table 2). ANME-2 are commonly found in cold seep environments with a shallow SMTZ associated with aragonite MDACs, whereas ANME-1 are found at greater depths typically associated with high-Mg calcite mineralogies (Peckmann et al., 2009; Guan et al., 2016; Yao et al., 2021; Iasakov et al., 2022). The syntrophic sulfate-reducing partner of ANME-2 belongs to the *Desulfosarcina/Desulfococcus* Seep-SRB1 cluster based on the *ai*-$C_{15:0}$/*i*-$C_{15:0}$ value <2 (Niemann and Elvert, 2008; Yao et al., 2021). The significant $^{13}$C-depletion in fatty acids derived from sulfate-reducing bacteria, i.e. *iso*- and *anteiso*-$C_{15}$ fatty acids (Table 2), is consistent with assimilation of methane-derived carbon. Intense microbial activity left typical petrographic features in the carbonate such as peloidal microfacies (Figure 3A) similar to other modern (Feng et al., 2008) and fossil methane-derived carbonates (Conti et al., 2010) and spherules possibly representing fossil sulfate-driven AOM aggregates (Himmler et al., 2022). In sample CarC-05, the vein filling displays three to five generations of cements separated by dissolution surfaces. Local corrosive conditions at methane seeps are commonly associated with aerobic methane oxidation (MoX) (Birgel et al., 2011; Himmler et al., 2011): $CH_4 + 2O_2 \rightarrow CO_2 + H_2O$. The carbon dioxide generated by MoX transforms into carbonic acid ($H_2CO_3$), and readily dissociates into bicarbonate ($HCO_3^-$) and/or carbonate ($CO_3^{2-}$) ions, releasing hydrogen ions. The consequent decrease in pH affects carbonate stability and favors its dissolution. The dissolution patterns are consistent with variations in seepage intensity and episodic establishment of oxygenated conditions favoring MoX. However, specific sterols of MoX bacteria, like 4,4-dimethyl and 4α-methyl sterols (Cordova-Gonzalez et al., 2020; Whiticar, 2020; Yao et al., 2021) were not identified, therefore the corrosion features may have been caused by other processes than MoX. Bacterial sulfide oxidation to sulfate ($H_2S + 2O_2 \rightarrow SO_4^{2-} + 2H^+$) is an alternative process that might have contributed to the generation of the corrosion surfaces and would explain the absence of pyrite in the sample (Figure 3) (Himmler et al., 2011; Leprich et al., 2021). Unfortunately, sulfur-oxidizing bacteria do not produce characteristic biomarkers (Peckmann et al., 2004); however, the high contents of *n*-$C_{16}$ and *n*-$C_{16:1}$ fatty acids and their rather high $\delta^{13}C$ values compared to biomarkers of sulfate reducers (Elvert et al., 2003) may be explained by mixed sources of these fatty acids, possibly including sulfur-oxidizing bacteria (Arning et al., 2008). The vein-filling cements CarC-05-C-*1*, CarC-05-C-*2*, CarC-05-C-*3* show varying, but low $\delta^{13}C$ values compared to non-seep marine carbonates which generally range from −7‰ to +8‰ (Judd and Hovland, 2007). These results indicate persistent methane oxidation in the pore waters, but a variable proportion of methane-derived carbon incorporated into the aragonite cements during growth due to dynamic seepage conditions (Roberts and Feng, 2013). These findings are consistent with a number of studies demonstrating that seepage activity can vary both spatially and temporally (Judd and Hovland, 2007; Suess, 2014; Ferré et al., 2020; Dølven et al., 2022), influencing subsurface biogeochemical processes (e.g. AOM, carbonate precipitation) (Rooze et al., 2020), the composition and distribution of seafloor chemosynthetic communities (Levin, 2005; Fischer et al., 2012) as well as local water-column biogeochemistry (Sert et al., 2020; Zhang et al., 2020; Gründger et al., 2021). We conducted thermodynamic modelling of the oxygen isotopic composition of aragonite cements forming in equilibrium with coeval bottom waters (8 ka BP and 4 ka BP) to check whether samples recorded some influence from gas hydrates. Assuming average bottom water temperatures of 4.3°C and 3°C (El bani Altuna et al., 2021), and seawater $\delta^{18}O$ SMOW of 0‰ (Fairbanks, 1989) we obtained aragonite $\delta^{18}O$ values of 3.9‰ and 4.2‰ (Kim et al., 2007). The obtained range of values of 4.6‰–5.3‰ is above the theoretical values and would correspond to temperatures below 1.2°C. Gas hydrates are not stable at this site at present-day pressure and temperature conditions and have not been stable since ~15 ka BP (Argentino et al., 2021). Fluids released by shallow gas hydrates take hundreds to few thousands of years to reach the seafloor in an advective system (Crémière et al., 2016; Serov et al., 2017), therefore an influence of gas hydrates for the examined aragonite cements is rather unlikely. A contribution of heavy, $^{18}$O-enriched water released by deep-related processes such as clay dehydration (Kastner et al., 1991) is not considered here, as there is no seismic evidence for deep warm fluid advection or opal-A to opal-CT transition in the upper sedimentary section of this area (cage.no). Stable isotope analyses of foraminiferal samples from the SW Barents Sea (Risebrobakken et al., 2010) indicated frequent temperature deviations of ±2°C–3°C from the mean bottom water temperatures throughout the Holocene, which might explain the variability of the obtained values, similarly to what was observed in late aragonitic phases from the Harstad Basin (Crémière et al., 2018). The $\delta^{13}C$ values measured in CarC-05-C-*1* and CarC-05-C-*2* are lower (−28.6‰ and −27.0‰, respectively) than the average isotopic composition of sedimentary organic matter in this area i.e. ca. −25‰ to −24‰ (Argentino et al., 2021), which is pointing to an incorporation of methane-derived carbon during precipitation. Evidence for the seepage of microbial methane stems from the

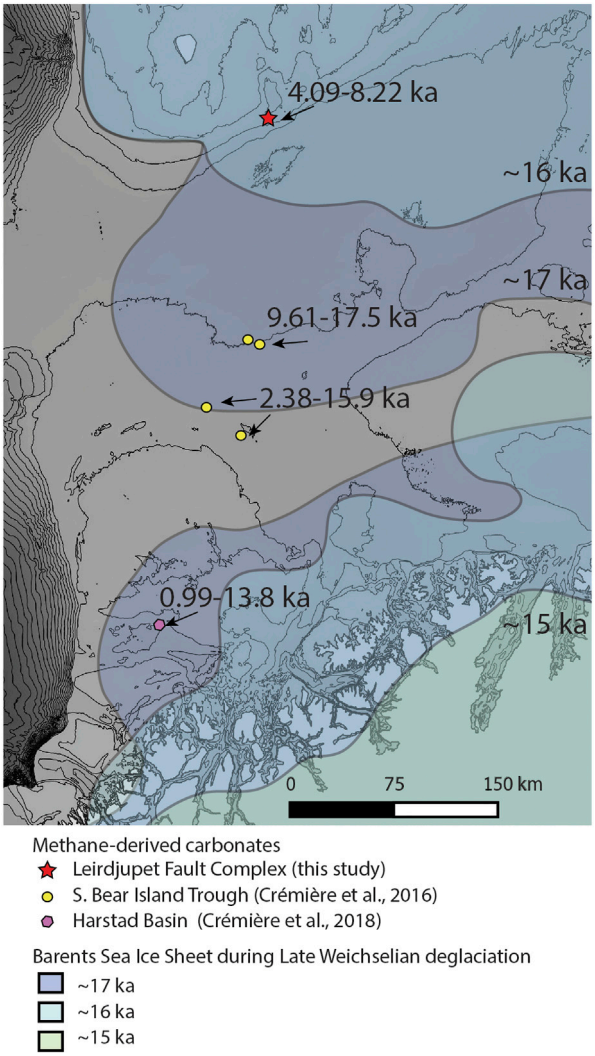


FIGURE 5
Location of methane-derived carbonate outcrops with available U/Th ages from the SW Barents Sea and approximated positions of the retreating ice-front at different stages of deglaciation of the Barents Sea Ice Sheet after Winsborrow et al., 2010.

carbon isotopic values of archaeol and *sn*2-hydroxy-archaeol with average $\delta^{13}C$ values of −122‰ (Table 2). These archaeal isoprenoids usually display a 50–70‰ offset for ANME-2 from the methane source (Niemann and Elvert, 2008), which is in agreement with biogenic methane, while the reported range of $\delta^{13}C_{methane}$ varies from −64.4‰ to −22.1‰ in this area (Argentino et al., 2021). Although the archaeal lipid biomarkers are not carrying a signature of thermogenic methane, the *n*-alkane distribution with a $CPI_{23\text{-}33}$ of 0.95 indicates the presence of traces of petroleum (*cf.* Marzi et al., 1993), which may contribute to the local presence of isotopically heavy methane. Mid- and long-chain *n*-alkanes carry a more or less uniform $\delta^{13}C$ values signature from −30‰ to −28‰, which is in the range of petroleum derived hydrocarbons (Supplementary Table S2). Overall, carbonate cements recorded a localized progressive decrease in AOM rates with the most negative $\delta^{13}C$ value associated with the early cements and the highest values in the last cement phase. This trend can be caused by the progressive clogging of fluid migration pathways through the formation of MDACs (Hovland, 2002) and lower methane inputs into the zone of carbonate precipitation, or to an overall decrease in upward migrating fluids from the deeper reservoirs. The latter scenario wassuggested by Argentino et al. (2021) based on the correlation of geochemical anomalies related to paleo-SMTZ (low $\delta^{13}C_{foraminifera}$, sulfur enrichments, barite fronts) in sediment cores at LFC. Our new isotopic data and U/Th ages from the carbonate samples support that interpretation and add additional time-constraints to the dynamics of methane seepage at the northern LFC in the pockmark site.

## Timing of carbonate formation and regional correlations

The SW Barents Sea hosts widespread sub-surface fluid plumbing systems consisting of shallow faults and fractures splaying from major deep-seated faults in hydrocarbon reservoirs or source rocks (Vadakkepuliyambatta et al., 2013). Surface expressions of fluid seepage such as pockmarks have been mapped over much of the Bear Island Trough, counting several hundred millions (Rise et al., 2014). The main phase of pockmark formation in the SW Barents Sea is hypothesized to have occurred during short-lived events (a few thousands of years) following the Late Weichselian ice-sheet retreat due to destabilization of gas hydrates. Although most of these features are no longer active (Chand et al., 2012; Mazzini et al., 2016), some are associated with active water-column gas flares indicating protracted seepage activity (Crémière et al., 2016, 2018). Detailed investigations of carbonate crusts associated with pockmarks in the SW Barents Sea have only been conducted for a few locations in the eastern Harstad Basin (Crémière et al., 2018) and SW Bear Island Trough (Crémière et al., 2016) and provided age ranges of 0.99–13.8 ka and 2.38–17.5 ka, respectively (Figure 5). Leirdjupet Fault Complex is located on the northern Bear Island Trough, 160–226 km north of the sites studied by Crémière et al. (2016). Paleo-hydrate destabilization in the pockmark area was suggested based on the combination of gas hydrate stability models and high $\delta^{18}O$ values in carbonate concretions from sediment cores and carbonate precipitation was constrained temporally to <14.5 ka BP by radiocarbon pinpoint and lithostratigraphy. Pore fluid datasets place the modern sulfate-methane transition along LFC between ~40 cm and ~110 cm below the seafloor whereas paleo-SMTZs have been identified by sediment proxies at shallower depths

indicating an overall decrease in methane fluxes (Argentino et al., 2021). The new U-Th dates provided here are indicating a protracted MDAC formation during the period from ~8 to ~4 ka, but also evidence active present-day seepage (ROV observation of methane bubbles and microbial mats). We suggest that AOM and resultant carbonate precipitation continued from ~14.5 ka until today, with only a few interruptions marked by local carbonate dissolution reflecting the occurrence of episodic oxidizing conditions. In particular, a major dissolution event occurred between the precipitation of phases CarC-05-C-2 and CarC-05-C-3 (Figures 4B, C), producing a hiatus of a few thousand years possibly related to deep processes acting on the migration of methane-rich fluids, e.g. fault-reactivation (Crémière et al., 2018). Since the carbonate sample was collected from the top of a carbonate outcrop, we are unable to extrapolate our interpretations to the entire carbonate deposits. We are also unable to trace the evolution of LFC deposits buried in the sediment. However, we know from glacial morphology reconstructions (Winsborrow et al., 2010) and thermomechanical ice-sheet models (Patton et al., 2017), that this area was covered by a grounded ice sheet until ca. 16 ka BP and the edge of gas hydrate stability crossed northern LFC at around 15 ka (Argentino et al., 2021). Therefore, the inception of seepage at LFC was tightly linked to the timing of grounded ice sheet retreat, and caused by the consequent gas hydrate destabilization and glacially-induced changes in stress fields (Argentino et al., 2021). The methane seepage history recorded in the methane-derived carbonates at LFC followed a similar evolution as in vicinal sites in the south (Crémière et al., 2016, 2018), chiefly controlled by the asynchronous deglaciation of the Barents Sea shelf areas, demonstrating that despite the overall decrease in seafloor gas expulsion recorded since last deglaciation, methane-derived carbonate precipitation is still an active process at many Arctic locations.

## Conclusion

Fault-controlled methane seepage at the Leirdjupet Fault complex has been detected along a ~35 km transect during CAGE expeditions in 2018 and 2021, representing one of the most active seepage areas in the SW Barents Sea. Seafloor imagery acquired using a remotely operated underwater vehicle enabled us to characterize the seabed features and chemosynthetic communities in a 120 x 220 m elongated pockmark, and to collect methane-derived carbonate samples to study biogeochemical processes associated with methane oxidation. Carbonates form $<10\ m^2$ bodies composed of vertically stacked slabs with a thickness of 20–30 cm, projecting as high as 2 m above the seafloor. White patches ($<1\ m^2$ wide) of bacterial mats only occur around the outer rim of carbonate crusts and around cm-sized cavities and cracks within the carbonates and not in surrounding sediments, pointing toward an effective sealing behavior of the carbonate deposits at this site. Microstructural analyses of vein-filling cements from a rock sample collected from the top of a carbonate body showed the occurrence of three to five generations of isopachous aragonitic cements separated by dissolution surfaces indicative of intermitted oxygenated conditions. Phase-specific stable isotope analysis and U/Th dating of aragonite cement revealed trend of decreasing $\delta^{13}C$ values with time, ranging from $\delta^{13}C = -28.6‰$ (early phase) to $\delta^{13}C = -10.1‰$ (late phase), which enabled us to trace anaerobic oxidation of methane from 8.223 ka to 4.087 ka. Molecular and compound-specific isotopic analysis of lipid biomarkers allowed the identification of ANME-2 archaea and Seep-SRB1 sulfate-reducing bacteria and the detection of traces of petroleum. This study provides new biogeochemical and temporal constraints on the inception and evolution of seepage at LFC, which can be used to correlate past methane emissions along the western Barents Sea margin.

## Data availability statement

The original contributions presented in the study are included in the article/Supplementary Material, further inquiries can be directed to the corresponding author.

## Author contributions

CA and GP conceived the study. CA and AL conducted microstructural analyses, LF conducted seafloor image aquisitions and processing. DS performed U/Th analyses. CA, DB and JP conducted sample preparation and analysis of biomarkers. All the authors contributed to the discussion and improvement of the manuscript and approved the article for submission.

## Funding

The research was supported by AKMA project (Research Council of Norway grant No. 287869) within the frame of the Centre for Arctic Gas Hydrate, Environment and Climate (CAGE) (Research Council of Norway grant No. 223259). Biomarker analyses were conducted during a research stay funded by Erasmus+ staff mobility 2021 granted to CA.

## Acknowledgments

We would like to acknowledge the captain and crew onboard R/V *Helmer Hanssen* and *Kronsprins Haakon* for the assistance

during the expeditions CAGE18-4, CAGE21-1-AKMA. We are grateful to Matteus Lindgren (UiT) for technical support in stable isotope analysis and Sabine Beckmann (Universität Hamburg) for support in the organic geochemistry laboratory. We acknowledge GC-IRMS measurements by Enno Schefuß and Ralph Kreutz (MARUM, Universität Bremen). We thank the two reviewers for their comments and suggestions that greatly improved the manuscript.

## Conflict of interest

The authors declare that the research was conducted in the absence of any commercial or financial relationships that could be construed as a potential conflict of interest.

## Publisher's note



## Supplementary material

The Supplementary Material for this article can be found online at: https://www.frontiersin.org/articles/10.3389/feart.2022.1029471/full#supplementary-material

## References

Aharon, P. (1994). Geology and biology of modern and ancient submarine hydrocarbon seeps and vents: An introduction. *Geo-Marine Lett.* 14, 69–73. doi:10.1007/BF01203716

Andreassen, K., Hubbard, A., Winsborrow, M., Patton, H., Vadakkepuliyambatta, S., Plaza-Faverola, A., et al. (2017). Massive blow-out craters formed by hydrate-controlled methane expulsion from the Arctic seafloor. *Science* 356 (80), 948–953. doi:10.1126/science.aal4500

Argentino, C., Conti, S., Fioroni, C., Fontana, D., Sciences, G., and Emilia, R. (2019). Evidences for paleo-gas hydrate occurrence: What we can infer for the miocene of the northern apennines (Italy). *Geosciences* 9, 134. doi:10.3390/geosciences9030134

Argentino, C., Savini, A., and Panieri, G. (2022). "Integrating fine-scale habitat mapping and pore water analysis in cold seep research: A case study from the SW Barents Sea," in *World atlas of submarine gas hydrates in continental margins* (Cham: Springer International Publishing), 505–514. doi:10.1007/978-3-030-81186-0_43

Argentino, C., Waghorn, K. A., Vadakkepuliyambatta, S., Polteau, S., Bünz, S., and Panieri, G. (2021). Dynamic and history of methane seepage in the SW Barents Sea: New insights from Leirdjupet Fault complex. *Sci. Rep.* 11, 4373. doi:10.1038/s41598-021-83542-0

Arning, E. T., Birgel, D., Schulz-Vogt, H. N., Holmkvist, L., Jørgensen, B. B., Larson, A., et al. (2008). Lipid biomarker patterns of phosphogenic sediments from upwelling regions. *Geomicrobiol. J.* 25, 69–82. doi:10.1080/01490450801934854

Birgel, D., and Peckmann, J. (2008). Aerobic methanotrophy at ancient marine methane seeps: A synthesis. *Org. Geochem.* 39, 1659–1667. doi:10.1016/j.orggeochem.2008.01.023

Bachmann, F., Hielscher, R., and Schaeben, H. (2010). Texture analysis with MTEX – free and open source software toolbox. *Solid State Phenom.* 160, 63–68. doi:10.4028/www.scientific.net/ssp.160.63

Bayon, G., Lemaitre, N., Barrat, J.-A., Wang, X., Feng, D., and Duperron, S. (2020). Microbial utilization of rare Earth elements at cold seeps related to aerobic methane oxidation. *Chem. Geol.* 555, 119832. doi:10.1016/j.chemgeo.2020.119832

Birgel, D., Feng, D., Roberts, H. H., and Peckmann, J. (2011). Changing redox conditions at cold seeps as revealed by authigenic carbonates from Alaminos Canyon, northern Gulf of Mexico. *Chem. Geol.* 285, 82–96. doi:10.1016/j.chemgeo.2011.03.004

Boetius, A., Ravenschlag, K., Schubert, C. J., Rickert, D., Widdel, F., Gieseke, A., et al. (2000). A marine microbial consortium apparently mediating anaerobic oxidation of methane. *Nature* 407, 623–626. doi:10.1038/35036572

Bohrmann, G., Greinert, J., Suess, E., and Torres, M. (1998). Authigenic carbonates from the Cascadia subduction zone and their relation to gas hydrate stability. *Geol.* 26, 647–650. doi:10.1130/0091-7613(1998)026<0647:acftcs>2.3.co;2

Bohrmann, G., Suess, E., Greinert, J., Teichert, B., and Naehr, T. (2002). Gas hydrate carbonates from Hydrate Ridge. cascadia convergent margin : Indicators of near-seafloor clathrate deposits gas hydrate carbonates from Hydrate Ridge. cascadia convergent margin : Indicators of near-seafloor clathrate deposits.

Bohrmann, G., and Torres, M. E. (2006). Gas hydrates in marine sediments. *Mar. Geochem.*, 481–512. doi:10.1007/3-540-32144-6_14

Bojanowski, M. J., Oszczypko-Clowes, M., Barski, M., Oszczypko, N., Radzikowska, M., and Ciesielska, Z. (2021). Slope destabilization provoked by dissociation of gas hydrates in the Outer Carpathian basin during the Oligocene: Sedimentological, petrographic, isotopic and biostratigraphic record. *Mar. Pet. Geol.* 123, 104585. doi:10.1016/j.marpetgeo.2020.104585

Campbell, K. A., Francis, D. A., Collins, M., Gregory, M. R., Nelson, C. S., Greinert, J., et al. (2008). Hydrocarbon seep-carbonates of a miocene forearc (East Coast basin), north Island, New Zealand. *Sediment. Geol.* 204, 83–105. doi:10.1016/j.sedgeo.2008.01.002

Campbell, K. a. (2006). Hydrocarbon seep and hydrothermal vent paleoenvironments and paleontology: Past developments and future research directions. *Palaeogeogr. Palaeoclimatol. Palaeoecol.* 232, 362–407. doi:10.1016/j.palaeo.2005.06.018

Casella, L. A., Griesshaber, E., Roda, M. S., Ziegler, A., Mavromatis, V., Henkel, D., et al. (2018). Micro- and nanostructures re fl ect the degree of diagenetic alteration in modern and fossil brachiopod shell calcite : A multi-analytical screening approach ( cl , FE-SEM , afm , EBSD ). *Palaeogeogr. Palaeoclimatol. Palaeoecol.* 502, 13–30. doi:10.1016/j.palaeo.2018.03.011

Cau, S., Franchi, F., Roveri, M., and Taviani, M. (2015). The Pliocene-age Stirone river hydrocarbon chemoherm complex (northern Apennines, Italy). *Mar. Pet. Geol.* 66, 582–595. doi:10.1016/j.marpetgeo.2015.05.027

Chand, S., Thorsnes, T., Rise, L., Brunstad, H., Stoddart, D., Bøe, R., et al. (2012). Multiple episodes of fluid flow in the SW Barents Sea (Loppa High) evidenced by gas flares, pockmarks and gas hydrate accumulation. *Earth Planet. Sci. Lett.* 332, 305–314. doi:10.1016/j.epsl.2012.03.021

Conti, S., Fontana, D., and Mecozzi, S. (2010). A contribution to the reconstruction of Miocene seepage from authigenic carbonates of the northern Apennines (Italy). *Geo-Mar. Lett.* 30, 449–460. doi:10.1007/s00367-010-0196-9

Conti, S., and Fontana, D. (1999). Miocene chemoherms of the northern Apennines, Italy. *Geology* 27, 927–930. doi:10.1130/0091-7613(1999)027<0927:MCOTNA>2.3.CO;2

Cordova-Gonzalez, A., Birgel, D., Kappler, A., and Peckmann, J. (2020). Carbon stable isotope patterns of cyclic terpenoids: A comparison of cultured alkaliphilic aerobic methanotrophic bacteria and methane-seep environments. *Org. Geochem.* 139, 103940. doi:10.1016/j.orggeochem.2019.103940

Crameri, F., Shephard, G. E., and Heron, P. J. (2020). The misuse of colour in science communication. *Nat. Commun.* 11, 5444–5510. doi:10.1038/s41467-020-19160-7

Crémière, A., Chand, S., Sahy, D., Thorsnes, T., Martma, T., Noble, S. R., et al. (2018). Structural controls on seepage of thermogenic and microbial methane since the last glacial maximum in the Harstad Basin, southwest Barents Sea. *Mar. Pet. Geol.* 98, 569–581. doi:10.1016/j.marpetgeo.2018.07.010

Crémière, A., Lepland, A., Chand, S., Sahy, D., Condon, D. J., Noble, S. R., et al. (2016). Timescales of methane seepage on the Norwegian margin following collapse

of the Scandinavian Ice Sheet. *Nat. Commun.* 7, 11509–11510. doi:10.1038/ncomms11509

Crémière, A., Pellerin, A., Wing, B. A., and Lepland, A. (2020). Multiple sulfur isotopes in methane seep carbonates track unsteady sulfur cycling during anaerobic methane oxidation. *Earth Planet. Sci. Lett.* 532, 115994–115998. doi:10.1016/j.epsl.2019.115994

Cusack, M., England, J., Dalbeck, P., Tudhope, A. W., Fallick, A. E., and Allison, N. (2008). Electron backscatter diffraction (EBSD) as a tool for detection of coral diagenesis. *Coral Reefs* 27, 905–911. doi:10.1007/s00338-008-0414-3

Davidson, D. W., Leaist, D. G., and Hesse, R. (1983). Oxygen-18 enrichment in the water of a clathrate hydrate. *Geochim. Cosmochim. Acta* 47, 2293–2295. doi:10.1016/0016-7037(83)90053-4

Dølven, K. O., Ferré, B., Silyakova, A., Jansson, P., Linke, P., and Moser, M. (2022). Autonomous methane seep site monitoring offshore Western svalbard: Hourly to seasonal variability and associated oceanographic parameters. *Ocean. Sci.* 18, 233–254. doi:10.5194/os-18-233-2022

El bani Altuna, N., Rasmussen, T. L., Ezat, M. M., Vadakkepuliyambatta, S., Groeneveld, J., and Greaves, M. (2021). Deglacial bottom water warming intensified Arctic methane seepage in the NW Barents Sea. *Commun. Earth Environ.* 2, 188–189. doi:10.1038/s43247-021-00264-x

Elverhøi, A., Siegert, M., Dowdeswell, J., and Svendsen, J.-I. (2002). The eurasian arctic during the last ice age. *Am. Sci.* 90, 32. doi:10.1511/2002.13.753

Elvert, M., Boetius, A., Knittel, K., and Jørgensen, B. B. (2003). Characterization of specific membrane fatty acids as chemotaxonomic markers for sulfate-reducing bacteria involved in anaerobic oxidation of methane. *Geomicrobiol. J.* 20, 403–419. doi:10.1080/01490450303894

Esteves, M., Bjarnadóttir, L. R., Winsborrow, M. C. M., Shackleton, C. S., and Andreassen, K. (2017). Retreat patterns and dynamics of the Sentralbankrenna glacial system, central Barents Sea. *Quat. Sci. Rev.* 169, 131–147. doi:10.1016/j.quascirev.2017.06.004

Fairbanks, R. G. (1989). A 17, 000-year glacio-eustatic sea level record: Influence of glacial melting rates on the younger dryas event and deep-ocean circulation. *Nature* 342, 637–642. doi:10.1038/342637a0

Fallati, L., Saponari, L., Savini, A., Marchese, F., Corselli, C., and Galli, P. (2020). Multi-temporal UAV data and object-based image analysis (OBIA) for estimation of substrate changes in a post-bleaching scenario on a Maldivian reef. *Remote Sens. (Basel).* 12, 2093. doi:10.3390/rs12132093

Feng, D., Chen, D. F., Qi, L., and Roberts, H. H. (2008). Petrographic and geochemical characterization of seep carbonate from Alaminos Canyon, Gulf of Mexico. *Sci. Bull. (Beijing).* 53, 1716–1724. doi:10.1007/s11434-008-0157-0

Feng, D., Chen, D., Peckmann, J., and Bohrmann, G. (2010a). Authigenic carbonates from methane seeps of the northern Congo fan: Microbial formation mechanism. *Mar. Pet. Geol.* 27, 748–756. doi:10.1016/j.marpetgeo.2009.08.006

Feng, D., Peng, Y., Bao, H., Peckmann, J., Roberts, H. H., and Chen, D. (2016). A carbonate-based proxy for sulfate-driven anaerobic oxidation of methane. *Geology* 44, 999–1002. doi:10.1130/G38233.1

Feng, D., Roberts, H. H., Cheng, H., Peckmann, J., Bohrmann, G., Lawrence Edwards, R., et al. (2010b). U/Th dating of cold-seep carbonates: An initial comparison. *Deep Sea Res. Part II Top. Stud. Oceanogr.* 57, 2055–2060. doi:10.1016/j.dsr2.2010.09.004

Ferré, B., Jansson, P. G., Moser, M., Serov, P., Portnov, A., Graves, C. A., et al. (2020). Reduced methane seepage from Arctic sediments during cold bottom-water conditions. *Nat. Geosci.* 13, 144–148. doi:10.1038/s41561-019-0515-3

Fischer, D., Sahling, H., Nöthen, K., Bohrmann, G., Zabel, M., and Kasten, S. (2012). Interaction between hydrocarbon seepage, chemosynthetic communities, and bottom water redox at cold seeps of the Makran accretionary prism: Insights from habitat-specific pore water sampling and modeling. *Biogeosciences* 9, 2013–2031. doi:10.5194/bg-9-2013-2012

Foucher, J. P., Westbrook, G. K., Boetius, A., Ceramicola, S., Dupré, S., Mascle, J., et al. (2007). Structure and drivers of cold seep ecosystems. *Oceanogr. Wash. D. C).* 22, 92–109. doi:10.5670/oceanog.2009.11

Greinert, J., Bohrmann, G., and Suess, E. (2001). Gas hydrate-associated carbonates and methane-venting at Hydrate Ridge: Classification, distribution, and origin of authigenic lithologies. *Geophys. Monogr. Ser.* 124, 99–113. doi:10.1029/GM124p0099

Greinert, J., Bohrmann, G., and Suess, E. (2013). Gas hydrate-associated carbonates and methane-venting at Hydrate Ridge: Classification, distribution, and origin of authigenic lithologies. *Geophys. Monogr. Ser.* 124, 99–113. doi:10.1029/GM124p0099

Gründger, F., Probandt, D., Knittel, K., Carrier, V., Kalenitchenko, D., Silyakova, A., et al. (2021). Seasonal shifts of microbial methane oxidation in Arctic shelf waters above gas seeps. *Limnol. Oceanogr.* 66, 1896–1914. doi:10.1002/lno.11731

Guan, H., Feng, D., Wu, N., and Chen, D. (2016). Methane seepage intensities traced by biomarker patterns in authigenic carbonates from the South China Sea. *Org. Geochem.* 91, 109–119. doi:10.1016/j.orggeochem.2015.11.007

Himmler, T., Bach, W., Bohrmann, G., and Peckmann, J. (2010). Rare Earth elements in authigenic methane-seep carbonates as tracers for fluid composition during early diagenesis. *Chem. Geol.* 277, 126–136. doi:10.1016/j.chemgeo.2010.07.015

Himmler, T., Brinkmann, F., Bohrmann, G., and Peckmann, J. (2011). Corrosion patterns of seep-carbonates from the eastern Mediterranean Sea. *Terra Nov.* 23, 206–212. doi:10.1111/j.1365-3121.2011.01000.x

Himmler, T., Crémière, A., Birgel, D., Wirth, R., Orphan, V. J., Kirsimäe, K., et al. (2022). Putative fossils of chemotrophic microbes preserved in seep carbonates from Vestnesa Ridge, off northwest Svalbard, Norway. *Geology* 50, 169–173. doi:10.1130/G49620.1

Himmler, T., Sahy, D., Martma, T., Bohrmann, G., Plaza-Faverola, A., Bünz, S., et al. (2019). A 160, 000-year-old history of tectonically controlled methane seepage in the Arctic. *Sci. Adv.* 5, eaaw1450. doi:10.1126/sciadv.aaw1450

Hinrichs, K.-U., and Boetius, A. (2002). "The anaerobic oxidation of methane: New insights in microbial ecology and biogeochemistry," in *Ocean margin systems* (Berlin, Heidelberg: Springer Berlin Heidelberg), 457–477. doi:10.1007/978-3-662-05127-6_28

Hinrichs, K.-U., Summons, R. E., Orphan, V., Sylva, S. P., and Hayes, J. M. (2000). Molecular and isotopic analysis of anaerobic methane-oxidizing communities in marine sediments. *Org. Geochem.* 31, 1685–1701. doi:10.1016/S0146-6380(00)00106-6

Hong, W. L., Torres, M. E., Carroll, J. L., Crémière, A., Panieri, G., Yao, H., et al. (2017). Erratum: Seepage from an arctic shallow marine gas hydrate reservoir is insensitive to momentary ocean warming. *Nat. Commun.* 8, 16126. doi:10.1038/ncomms16126

Hovland, M. (2002). On the self-sealing nature of marine seeps. *Cont. Shelf Res.* 22, 2387–2394. doi:10.1016/S0278-4343(02)00063-8

Iasakov, T. R., Kanapatskiy, T. A., Toshchakov, S. V., Korzhenkov, A. A., Ulyanova, M. O., and Pimenov, N. V. (2022). The Baltic Sea methane pockmark microbiome: The new insights into the patterns of relative abundance and ANME niche separation. *Mar. Environ. Res.* 173, 105533. doi:10.1016/j.marenvres.2021.105533

Jansson, P., Triest, J., Grilli, R., Ferré, B., Silyakova, A., Mienert, J., et al. (2019). High-resolution underwater laser spectrometer sensing provides new insights into methane distribution at an Arctic seepage site. *Ocean. Sci.* 15, 1055–1069. doi:10.5194/os-15-1055-2019

Judd, A. G., and Hovland, M. (2007). Seabed fluid flow: The impact of geology, biology and the marine environment. doi:10.1007/s00254-004-1086-0

Judd, A., Noble-James, T., Golding, N., Eggett, A., Diesing, M., Clare, D., et al. (2020). The croker carbonate slabs: Extensive methane-derived authigenic carbonate in the Irish sea—nature, origin, longevity and environmental significance. *Geo-Mar. Lett.* 40, 423–438. doi:10.1007/s00367-019-00584-0

Kastner, M., Elderfield, H., and Martin, J. B. (1991). Fluids in convergent margins: What do we know about their composition, origin, role in diagenesis and importance for oceanic chemical fluxes? *Philos. Trans. - R. Soc. Lond. A* 335, 243–259. doi:10.1098/rsta.1991.0045

Kim, B., and Zhang, Y. G. (2022). Methane hydrate dissociation across the Oligocene–Miocene boundary. *Nat. Geosci.* 15, 203–209. doi:10.1038/s41561-022-00895-5

Kim, S., Neil, J. R. O., Hillaire-marcel, C., and Mucci, A. (2007). Oxygen isotope fractionation between synthetic aragonite and water : Influence of temperature and Mg2 + concentration Oxygen isotope fractionation between synthetic aragonite and water : Influence of temperature and Mg 2 + concentration. doi:10.1016/j.gca.2007.04.019

Knittel, K., and Boetius, A. (2009). Anaerobic oxidation of methane: Progress with an unknown process. *Annu. Rev. Microbiol.* 63, 311–334. doi:10.1146/annurev.micro.61.080706.093130

Kravchishina, M. D., Lein, A. Y., Flint, M. V., Baranov, B. V., Miroshnikov, A. Y., Dubinina, E. O., et al. (2021). Methane-derived authigenic carbonates on the seafloor of the laptev Sea shelf. *Front. Mar. Sci.* 8. doi:10.3389/fmars.2021.690304

Leprich, D. J., Flood, B. E., Schroedl, P. R., Ricci, E., Marlow, J. J., Girguis, P. R., et al. (2021). Sulfur bacteria promote dissolution of authigenic carbonates at marine methane seeps. *ISME J.* 15, 2043–2056. doi:10.1038/s41396-021-00903-3

Levin, L. a. (2005). Ecology of cold seep sediments : Interactions of fauna with flow , chemistry and microbes. *Oceanogr. Mar. Biol. Annu. Rev.* 43, 1–46. doi:10.1201/9781420037449.ch1

Levin, L. A., Baco, A. R., Bowden, D. A., Colaco, A., Cordes, E. E., Cunha, M. R., et al. (2016). Hydrothermal vents and methane seeps: Rethinking the sphere of influence. *Front. Mar. Sci.* 3, 1–23. doi:10.3389/fmars.2016.00072

Loher, M., Marcon, Y., Pape, T., Römer, M., Wintersteller, P., dos Santos Ferreira, C., et al. (2018). Seafloor sealing, doming, and collapse associated with gas seeps and authigenic carbonate structures at Venere mud volcano, Central Mediterranean. *Deep Sea Res. Part I Oceanogr. Res. Pap.* 137, 76–96. doi:10.1016/j.dsr.2018.04.006

Lu, Y., Sun, X., Xu, H., Konishi, H., Lin, Z., Xu, L., et al. (2018). Formation of dolomite catalyzed by sulfate-driven anaerobic oxidation of methane: Mineralogical and geochemical evidence from the northern South China Sea. *Am. Mineral.* 103, 720–734. doi:10.2138/am-2018-6226

Magalhães, V. H., Pinheiro, L. M., Ivanov, M. K., Kozlova, E., Blinova, V., Kolganova, J., et al. (2012). Formation processes of methane-derived authigenic carbonates from the Gulf of Cadiz. *Sediment. Geol.* 243–244, 155–168. doi:10.1016/j.sedgeo.2011.10.013

Marlow, J. J., Steele, J. A., Ziebis, W., Thurber, A. R., Levin, L. A., and Orphan, V. J. (2014). Carbonate-hosted methanotrophy represents an unrecognized methane sink in the deep sea. *Nat. Commun.* 5, 5094. doi:10.1038/ncomms6094

Marzi, R., Torkelson, B. E., and Olson, R. K. (1993). A revised carbon preference index. *Org. Geochem.* 20, 1303–1306. doi:10.1016/0146-6380(93)90016-5

Mayorga, I. C., Astilleros, J. M., and Fernández-Díaz, L. (2019). Precipitation of caco 3 polymorphs from aqueous solutions: The role of ph and sulphate groups. *Minerals* 9, 178–216. doi:10.3390/min9030178

Mazzini, A., Svensen, H. H., Planke, S., Forsberg, C. F., and Tjelta, T. I. (2016). Pockmarks and methanogenic carbonates above the giant Troll gas field in the Norwegian North Sea. *Mar. Geol.* 373, 26–38. doi:10.1016/j.margeo.2015.12.012

McGinnis, D. F., Greinert, J., Artemov, Y., Beaubien, S. E., and Wüest, A. (2006). Fate of rising methane bubbles in stratified waters: How much methane reaches the atmosphere? *J. Geophys. Res.* 111, C09007. doi:10.1029/2005JC003183

Meyers, P. A. (1994). Preservation of elemental and isotopic source identification of sedimentary organic matter. *Chem. Geol.* 114, 289–302. doi:10.1016/0009-2541(94)90059-0

Michaelis, W., Seifert, R., Nauhaus, K., Treude, T., Thiel, V., Blumenberg, M., et al. (2002). Microbial reefs in the Black Sea fueled by anaerobic oxidation of methane. *Science* 297, 1013–1015. doi:10.1126/science.1072502

Montalbetti, E., Fallati, L., Casartelli, M., Maggioni, D., Montano, S., Galli, P., et al. (2022). Reef complexity influences distribution and habitat choice of the corallivorous seastar Culcita schmideliana in the Maldives. *Coral Reefs* 41, 253–264. doi:10.1007/s00338-022-02230-1

Niemann, H., and Elvert, M. (2008). Diagnostic lipid biomarker and stable carbon isotope signatures of microbial communities mediating the anaerobic oxidation of methane with sulphate. *Org. Geochem.* 39, 1668–1677. doi:10.1016/j.orggeochem.2007.11.003

Panieri, G., Bünz, S., Fornari, D. J., Escartin, J., Serov, P., Jansson, P., et al. (2017). An integrated view of the methane system in the pockmarks at Vestnesa Ridge, 79°N. *Mar. Geol.* 390, 282–300. doi:10.1016/j.margeo.2017.06.006

Patton, H., Hubbard, A., Andreassen, K., Auriac, A., Whitehouse, P. L., Stroeven, A. P., et al. (2017). Deglaciation of the Eurasian ice sheet complex. *Quat. Sci. Rev.* 169, 148–172. doi:10.1016/j.quascirev.2017.05.019

Peckmann, J., Birgel, D., and Kiel, S. (2009). Molecular fossils reveal fluid composition and flow intensity at a Cretaceous seep. *Geology* 37, 847–850. doi:10.1130/G25658A.1

Peckmann, J., and Thiel, V. (2004). Carbon cycling at ancient methane-seeps. *Chem. Geol.* 205, 443–467. doi:10.1016/j.chemgeo.2003.12.025

Peckmann, J., Thiel, V., Reitner, J., Taviani, M., Aharon, P., and Michaelis, W. (2004). A microbial mat of a large sulfur bacterium preserved in a miocene methane-seep limestone. *Geomicrobiol. J.* 21, 247–255. doi:10.1080/01490450490438757

Phrampus, B. J., Lee, T. R., and Wood, W. T. (2020). A global probabilistic prediction of cold seeps and associated SEAfloor FLuid expulsion anomalies (SEAFLEAs). *Geochem. Geophys. Geosyst.* 21. doi:10.1029/2019GC008747

Pierre, C., Demange, J., Blanc-Valleron, M. M., and Dupré, S. (2017). Authigenic carbonate mounds from active methane seeps on the southern Aquitaine Shelf (Bay of Biscay, France): Evidence for anaerobic oxidation of biogenic methane and submarine groundwater discharge during formation. *Cont. Shelf Res.* 133, 13–25. doi:10.1016/j.csr.2016.12.003

Pierre, C., and Fouquet, Y. (2007). Authigenic carbonates from methane seeps of the Congo deep-sea fan. *Geo-Mar. Lett.* 27, 249–257. doi:10.1007/s00367-007-0081-3

Pierre, C., and Rouchy, J. M. (2004). Isotopic compositions of diagenetic dolomites in the Tortonian marls of the Western Mediterranean margins: Evidence of past gas hydrate formation and dissociation. *Chem. Geol.* 205, 469–484. doi:10.1016/j.chemgeo.2003.12.026

Portnov, A., Vadakkepuliyambatta, S., Mienert, J., and Hubbard, A. (2016). Ice-sheet-driven methane storage and release in the Arctic. *Nat. Commun.* 7, 10314. doi:10.1038/ncomms10314

Reeburgh, W. S. (2007). Oceanic methane biogeochemistry. *Chem. Rev.* 107, 486–513. doi:10.1021/cr050362v

Rise, L., Bellec, V. K., Ch, S., and Bøe, R. (2014). Pockmarks in the southwestern Barents Sea and finnmark fjords. *Nor. Geol. Tidsskr.* 94, 263–282. doi:10.17850/njg94-4-02

Risebrobakken, B., Moros, M., Ivanova, E. V., Chistyakova, N., and Rosenberg, R. (2010). Climate and oceanographic variability in the SW Barents Sea during the Holocene. *Holocene* 20, 609–621. doi:10.1177/0959683609356586

Roberts, H. H., and Feng, D. (2013). 3. Carbonate precipitation at Gulf of Mexico hydrocarbon seeps: An overview. *Hydrocarb. Seepage*, 43–61. doi:10.1190/1.9781560803119.ch3

Rooze, J., Peterson, L., Peterson, R. N., and Meile, C. (2020). Porewater flow patterns in surficial cold seep sediments inferred from conservative tracer profiles and early diagenetic modeling. *Chem. Geol.* 536, 119468. doi:10.1016/j.chemgeo.2020.119468

Sahling, H., Rickert, D., Lee, R. W., Linke, P., and Suess, E. (2002). Macrofaunal community structure and sulfide flux at gas hydrate deposits from the Cascadia convergent margin, NE Pacific. *Mar. Ecol. Prog. Ser.* 231, 121–138. doi:10.3354/meps231121

Sauer, S., Knies, J., Lepland, A., Chand, S., Eichinger, F., and Schubert, C. J. (2015). Hydrocarbon sources of cold seeps off the Vesterålen coast, northern Norway. *Chem. Geol.* 417, 371–382. doi:10.1016/j.chemgeo.2015.10.025

Schneider, A., Panieri, G., Lepland, A., Consolaro, C., Forwick, M., Johnson, J. E., et al. (2018). Methane seepage at vestnesa ridge ( NW svalbard ) since the last glacial maximum. *Quat. Sci. Rev.* 193, 98–117. doi:10.1016/j.quascirev.2018.06.006

Serov, P., Vadakkepuliyambatta, S., Mienert, J., Patton, H., Portnov, A., Silyakova, A., et al. (2017). Postglacial response of Arctic Ocean gas hydrates to climatic amelioration. *Proc. Natl. Acad. Sci. U. S. A.* 114, 6215–6220. doi:10.1073/pnas.1619288114

Sert, M. F., D'Andrilli, J., Gründger, F., Niemann, H., Granskog, M. A., Pavlov, A. K., et al. (2020). Compositional differences in dissolved organic matter between Arctic cold seeps versus non-seep sites at the Svalbard continental margin and the Barents Sea. *Front. Earth Sci.* 8 (8), 552731. doi:10.3389/feart.2020.552731

Smrzka, D., Feng, D., Himmler, T., Zwicker, J., Hu, Y., Monien, P., et al. (2020). Trace elements in methane-seep carbonates: Potentials, limitations, and perspectives. *Earth. Sci. Rev.* 208, 103263. doi:10.1016/j.earscirev.2020.103263

Smrzka, D., Zwicker, J., Klügel, A., Monien, P., Bach, W., Bohrmann, G., et al. (2016). Establishing criteria to distinguish oil-seep from methane-seep carbonates. *Geology* 44, 667–670. doi:10.1130/G38029.1

Sparrow, K. J., Kessler, J. D., Southon, J. R., Garcia-Tigreros, F., Schreiner, K. M., Ruppel, C. D., et al. (2018). Limited contribution of ancient methane to surface waters of the u.S. Beaufort sea shelf. *Sci. Adv.* 4, eaao4842–8. doi:10.1126/sciadv.aao4842

Suess, E. (2014). Marine cold seeps and their manifestations: Geological control, biogeochemical criteria and environmental conditions. doi:10.1007/s00531-014-1010-0

Suess, E. (2018). "Marine cold seeps: Background and recent advances," in *Hydrocarbons, oils and lipids: Diversity, origin, chemistry and fate* (Cham: Springer International Publishing), 1–21. doi:10.1007/978-3-319-54529-5_27-1

Swart, P. K. (2015). The geochemistry of carbonate diagenesis: The past, present and future. *Sedimentology* 62, 1233–1304. doi:10.1111/sed.12205

Teichert, B. M. A., Eisenhauer, A., Bohrmann, G., Haase-Schramm, A., Bock, B., and Linke, P. (2003). U/Th systematics and ages of authigenic carbonates from Hydrate Ridge, Cascadia Margin: Recorders of fluid flow variations. *Geochim. Cosmochim. Acta* 67, 3845–3857. doi:10.1016/S0016-7037(03)00128-5

Teichert, B. M. A. A., Bohrmann, G., and Suess, E. (2005a). Chemoherms on Hydrate Ridge — unique microbially-mediated carbonate build-ups growing into the water column. *Palaeogeogr. Palaeoclimatol. Palaeoecol.* 227, 67–85. doi:10.1016/j.palaeo.2005.04.029

Teichert, B. M. A., Gussone, N., Eisenhauer, A., and Bohrmann, G. (2005b). Clathrites: Archives of near-seafloor pore-fluid evolution (δ44/40Ca, δ13C, δ18O) in gas hydrate environments. *Geol.* 33, 213–216. doi:10.1130/G21317.1

Vadakkepuliyambatta, S., Bünz, S., Mienert, J., and Chand, S. (2013). Distribution of subsurface fluid-flow systems in the SW Barents Sea. *Mar. Pet. Geol.* 43, 208–221. doi:10.1016/j.marpetgeo.2013.02.007

Vadakkepuliyambatta, S., Chand, S., and Bünz, S. (2017). The history and future trends of ocean warming-induced gas hydrate dissociation in the SW Barents Sea. *Geophys. Res. Lett.* 44, 835–844. doi:10.1002/2016GL071841

Waage, M., Serov, P., Andreassen, K., Waghorn, K. A., and Bünz, S. (2020). Geological controls of giant crater development on the Arctic seafloor. *Sci. Rep.* 10, 1–12. doi:10.1038/s41598-020-65018-9–

Weber, T., Wiseman, N. A., and Kock, A. (2019). Global ocean methane emissions dominated by shallow coastal waters. *Nat. Commun.* 10, 4584. doi:10.1038/s41467-019-12541-7

Whiticar, M. J. (2020). "The biogeochemical methane cycle," in *Hydrocarbons, oils and lipids: Diversity, origin, chemistry and fate* (Cham: Springer International Publishing), 1–78. doi:10.1007/978-3-319-54529-5_5-1

Winsborrow, M. C. M., Andreassen, K., Corner, G. D., and Laberg, J. S. (2010). Deglaciation of a marine-based ice sheet: Late Weichselian palaeo-ice dynamics and retreat in the southern Barents Sea reconstructed from onshore and offshore glacial geomorphology. *Quat. Sci. Rev.* 29, 424–442. doi:10.1016/j.quascirev.2009.10.001

Yao, H., Niemann, H., and Panieri, G. (2020). Multi-proxy approach to unravel methane emission history of an Arctic cold seep. *Quat. Sci. Rev.* 244, 106490. doi:10.1016/j.quascirev.2020.106490

Yao, H., Panieri, G., Lehmann, M. F., Himmler, T., and Niemann, H. (2021). Biomarker and isotopic composition of seep carbonates record environmental conditions in two arctic methane seeps. *Front. Earth Sci.* 8, 1–12. doi:10.3389/feart.2020.570742

Zhang, Y., Jing, H., and Peng, X. (2020). Vertical shifts of particle-attached and free-living prokaryotes in the water column above the cold seeps of the South China Sea. *Mar. Pollut. Bull.* 156, 111230. doi:10.1016/j.marpolbul.2020.111230

Zwicker, J., Smrzka, D., Himmler, T., Monien, P., Gier, S., Goedert, J. L., et al. (2018). Rare Earth elements as tracers for microbial activity and early diagenesis: A new perspective from carbonate cements of ancient methane-seep deposits. *Chem. Geol.* 501, 77–85. doi:10.1016/j.chemgeo.2018.10.010